PAPER

Check for updates

Structural distortion-induced monoclinic sodium iron hexacyanoferrate as a high-performance electrode for rocking-chair desalination batteries†

Yuliang Wu,[a] Junkun Huang,[a] Chaolin Li [ID] [a,b] and Wenhui Wang [ID] *[a,b]

Sodium iron hexacyanoferrate (NaFeHCF) has been recognized as a promising Prussian blue analogue (PBA)-based electrode for electrochemical desalination; however, its application potential is limited by its unsatisfactory desalination capacity and cycling stability. Herein, the structurally distorted high-quality monoclinic NaFeHCF with fewer defects in the framework was synthesized by a crystal-controlled coprecipitation method *via* tuning the crystallization reaction conditions and applied to seawater desalination. Physicochemical characterization and desalination experiments show that the NFHFC-2 with minimized defects possesses enhanced electrochemical activity of Fe^{2+} and electrochemical kinetics, thus achieving higher desalination performance (specific capacity of 75.0 mA h g^{-1} and capacity retention of 85.3% after 50 cycles). Furthermore, a symmetrical NFHCF-2 RCDB is assembled, and the operation parameters (including various salinities and electrode spacing) are optimized to achieve a remarkable salt removal capacity (SRC) of 108.9 mg g^{-1} and a salt removal rate (SRR) of 2.22 mg g^{-1} min^{-1} with low energy consumption (0.056 kW h kg^{-1}-NaCl) and outstanding cycling stability (almost no capacity attenuation in 150 cycles). Impressively, the RCDB further exhibits favorable technical feasibility in the simultaneous removal of univalent/bivalent ions from the natural seawater. This study inspires the design of high-quality PBA-based electrodes with optimized crystal structures for electrochemical desalination.

1. Introduction

Industrial expansion and irrational utilization of freshwater have led to an increasingly serious freshwater resource scarcity.[1] Given that the ocean accounts for over 97% of the global water resources, seawater desalination, as an open-source and incremental technology for freshwater resources, has become an important way to solve the global freshwater crisis.[2] Although several conventional desalination technologies, such as reverse osmosis,[3] electrodialysis,[4] thermal evaporation,[5] and multistage flash distillation[6] have been widely applied, alternative strategies with features such as a low environmental footprint and low energy consumption are still required.

Capacitive deionization (CDI) technology is an emerging and promising electrochemical desalination process that enables ion storage by constructing an electric double layer at the electrode/solution interface.[7,8] However, the conventional carbon-based CDI system based on the non-faradaic ion storage mechanism results in a limited desalination capacity (<15 mg g^{-1}) and low charge efficiency in high-salinity aqueous media due to the co-ion expulsion effect.[9,10] To address the above issues, a desalination battery (DB) that uses battery-type electrodes was proposed in 2012, which could obtain high desalination performance through faradaic ion storage mechanisms even in high-salinity aqueous media.[11] A typical DB system usually consists of a sodium storage electrode and a chlorine storage electrode, but the shortage of sustainable high-performance chlorine storage electrodes has restricted its application potential.[12–15] Fortunately, the delicately designed rocking chair desalination battery (RCDB) architecture based on two sodium storage electrodes and an anion-exchange membrane can tackle the challenge.[16] Therefore, it is significant to develop sodium storage electrodes with outstanding electrochemical desalination performance.

Prussian blue analogues (PBA) have been widely investigated in various fields (rechargeable batteries, electrocatalysis, electrochemical desalination, *etc.*) due to their open framework structure capable of fast ion diffusion.[17,18] As a typical PBA, sodium iron hexacyanoferrate (NaFeHCF) is regarded as a promising material for DB thanks to its low cost, environmental friendliness, and facile, scalable production process.[19]

[a]School of Civil and Environmental Engineering, Harbin Institute of Technology, Shenzhen, Shenzhen 518055, China. E-mail: wangwenhui@hit.edu.cn
[b]State Key Laboratory of Urban Water Resource and Environment, Harbin Institute of Technology, Harbin 150090, China
†Electronic supplementary information (ESI) available. See DOI: https://doi.org/10.1039/d3nr04098d

However, NaFeHCF suffers from mediocre desalination capacity and poor cyclic stability.[20] Most previous studies have focused on improving the desalination performance of NaFeHCF by conductive layer coating and/or metal-ion (*e.g.*, Co, Ni, Cu, *etc*.) doping, but these methods often involve complex synthesis steps.[21–26]

On the other hand, it has been found that the electrochemical properties of PBA are closely related to its intrinsic crystal structure. Due to the rapid growth of crystals during the preparation process, a large number of $Fe(CN)_6$ vacancies and heterogeneous molecules (*e.g.*, interstitial water) are usually generated in the PBA framework, which will decrease host sites for Na^+, retard electron/ion transport, and impair the crystal periodicity, making the framework easy to collapse.[27,28] To address the above issues, some advanced reports have been devoted to preparing high-quality and well-crystallized PBA. For instance, Mai *et al.*[29] introduced a chelating agent in the hydrothermal process to reduce the crystallization rate and obtained a highly crystalline monoclinic PBA with excellent rate performance in nonaqueous sodium-ion batteries. It is reported that PBA with low vacancies, low interstitial water content, and high Na content often exhibit a monoclinic structure with low symmetry rather than a cubic structure, due to the crystal distortion, and show a higher capacity and long-term cyclability for nonaqueous sodium-ion batteries than those of cubic phase.[30,31] Nevertheless, to the best of our knowledge, the desalination behavior of NaFeHCF with low defects has not yet been explored.

Herein, monoclinic NaFeHCF with low defects was synthesized *via* a facile crystallization-controlled co-precipitation method. Insights into the influences of synthesis conditions on the crystal structure, electrochemical properties, and desalination performances of NaFeHCF were investigated. Moreover,

Dr Wenhui Wang is an associate professor at Harbin Institute of Technology, Shenzhen. He received his Bachelor's degree and Ph.D. from Harbin Institute of Technology and The Chinese University of Hong Kong, respectively. His research interests include Li/Na-ion batteries, seawater desalination, seawater Li mining, and advanced oxidation processes for wastewater treatment. He has published more than 50 papers as (co-)first/

Wenhui Wang

corresponding author in Appl. Catal. B: Environ., Energy Storage Mater., Water Res., etc. He is the recipient of the Eco-environment Youth Science and Technology Award of the Guangdong Environmental Science Society, the Guangdong Environmental Protection Science and Technology Award, and the Shenzhen Science and Technology Progress Award, among others.

a NaFeHCF∥NaFeHCF symmetrical RCDB was assembled to demonstrate its application potential, and the effects of various initial salinities and electrode spacing on its desalination performance and energy consumption were further investigated. Finally, the technical feasibility of the RCDB for natural seawater desalination was evaluated. This crystallization-controlled strategy paves a new way for the rational design of other PBA-based materials to achieve high-performance electrochemical desalination.

2. Experimental section

A detailed description of material preparation, desalination experiments, and characterization is given in the ESI.†

3. Results and discussion

3.1 Characterization

Since the chelating agent amount and reaction temperature will affect the crystallization rate during the precipitation process and thus control the density of lattice defects, their effect on the crystal structure and desalination performance of NaFeHCF was first optimized. It can be found that the as-synthesized NaFeHCF exhibits a monoclinic structure with high crystallinity when the chelating agent dose and the reaction temperature are 0.3 M and 60 °C, respectively, which delivers superior desalination capacity and cycle performance (detailed information, see Fig. S1 and 2†). Following the above optimal synthesis parameters, the crystal structure of NaFeHCF was tuned by adding an extra sodium source (NaCl), and then the relationship between crystal structure (defects) and desalination performance of NaFeHCF was revealed.

Fig. 1A exhibits the X-ray powder diffractometry (XRD) patterns of the as-synthesized NaFeHCF with different NaCl doses (NFHCF-*x*). The XRD pattern of NFHCF-0 can be indexed to the face-centered cubic structure of Prussian blue (JCPDS no. 73-0687). Through adding extra NaCl, several diffraction peaks, such as at $2\theta = 24°$, $39°$, $50°$, and $56°$, split into double peak structures, indicating the change in crystal structure from cubic to monoclinic due to the distortion. It is believed the structural change should be rooted in a high-content Na^+ occupying the lattice positions, which reduces the interstitial water molecules in the PBA framework.[32] With the increased dose of NaCl to 2 M, the diffraction peaks of the monoclinic phase show an increased relative intensity. However, further increasing NaCl doses to ≥3 M results in a reduced crystallinity of NaFeHCF. This is because excessive NaCl accelerates the crystallization rate of NaFeHCF, making some of the Na^+ unable to diffuse fast enough to reach the crystal position in time. As a result, water molecules will serve as a substitute in the crystal lattice to neutralize the charges arising from defective octahedrons, thus reducing the crystallinity of NaFeHCF.

According to the scanning electron microscopy (SEM) and transmission electron microscopy (TEM) images, the NFHCF-0

presents a cube morphology with a particle size of <1.2 μm. With the increased dose of NaCl to 2 M, the particle size of the samples increases, and the cubic shape becomes more obvious (Fig. 1 and S3†). When the NaCl dose increased to ≥3 M, part of the materials collapsed into small particles with irregular shapes and aggregates. As shown in Fig. 1C, the high-resolution TEM (HRTEM) image of NFHCF-0 exhibits a lattice fringe of 0.263 nm, corresponding to the (400) plane of Prussian blue. Whereas the lattice spacing of NFHCF-2 increases to 0.278 nm as induced by the structural distortion (Fig. 1E). The elemental mapping (EDS) images reveal that Na, Fe, C, and N scatter uniformly on NFHCF-2 (Fig. 1F–I).

Based on the cause of lattice defects in PBA as shown in the introduction, the lattice defect degree in NaFeHCF should be closely related to the content of interstitial water and Fe^{2+} (or Na^+ amount) in the material framework. Thus, thermogravimetric analysis (TGA) tests and X-ray photoelectron spectroscopy (XPS) were conducted to determine the interstitial water content and Fe^{2+} (or Na^+ amount) in the NFHCF-x, thus reflecting their defect degrees. As shown in Fig. 2A, the weight loss of NFHCF-0 was 0.34% (adsorbed water) and 14.9% (interstitial water), respectively. However, the interstitial water content of NFHCF-1/2/3/4 with monoclinic structure was significantly lower than that of NFHCF-0 with cubic structure, implying that the abundant Na^+ suppresses the occupation of water molecules in crystals. The interstitial water content of NFHCF-2 was only 10.5%, indicating a higher Na^+ content in the NaFeHCF framework.

XPS was further conducted to investigate the chemical composition and oxidation states of NFHCF-x. The XPS survey of all NFHCF-x demonstrated the existence of C, N, Fe, Na, and O elements (Fig. 2B). As shown in Fig. 2C, the high-resolution Fe 2p spectrum of NFHCF-x can be deconvoluted into four peaks attributed to Fe^{2+} (708.6 eV and 721.4 eV) and Fe^{3+} (710.9 eV and 724.1 eV), respectively.[33,34] It can be observed that the Fe^{2+} content increases from 51.2% for NFHCF-0 to 67.7% for NFHCF-2 due to the valence balance caused by the higher Na^+ content within the NaFeHCF framework. However, with the addition of excessive NaCl (≥3 M), Fe^{2+} content gradually decreases to 56.7% for NFHCF-3 and 52.0% for NFHCF-4, respectively. The Na^+ content in NFHCF-x was further investigated via ICP-OES analysis (Fig. 2D). It can be found that NFHCF-2 has a higher Na^+ content of 7.89 wt%, which is positively correlated with the Fe^{2+} content in XPS.

The redox reaction process of NFHCF-x was analyzed by cyclic voltammetry (CV) measurements in Fig. 2E. The redox peaks at around −0.07/0.01 V and 0.03/0.16 V for NFHCF-x are related to redox reactions of Fe^{3+}/Fe^{2+}. Compared with NFHCF-0, the peak current density of NFHCF-2 is obviously improved, corresponding to the higher electrochemical performance. To investigate the effect of crystal structure on the charge transfer kinetics of electrodes, electrochemical impedance spectra (EIS) were performed (Fig. S4 and Table S2†). The charge transfer resistance (R_{ct}) of NFHCF-0 is determined to be 12.0 Ω, which is obviously higher than those of NFHCF-1/2/3/4 due to the presence of plentiful vacancies and interstitial water in its cubic structure, impeding the electronic/ionic transfer pathway. Thus, the PBA with fewer vacancies and interstitial water is expected to have higher ionic diffusion ecoefficiency. In this regard, the D_{Na} is calculated based on the EIS (calculation process shown in the ESI†), and the results are 2.07×10^{-9}, 2.86×10^{-9}, 3.17×10^{-9}, 1.37×10^{-9}, and 1.03×10^{-9} cm^2 s^{-1} for NFHCF-0/1/2/3/4, respectively (Fig. 2F). The D_{Na} results are consistent with the above results
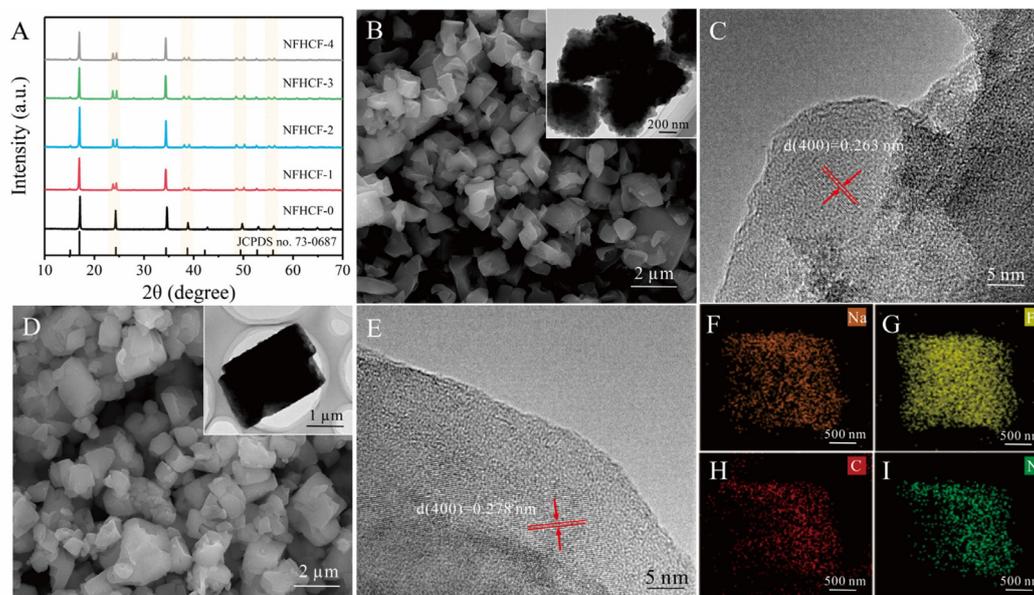

Fig. 1   (A) XRD patterns of NFHCF-x. (B) SEM, TEM images, and (C) HRTEM image of NFHCF-0. (D) SEM, TEM images, and (E) HRTEM image of NFHCF-2. (F–I) Elemental mapping images of NFHCF-2.
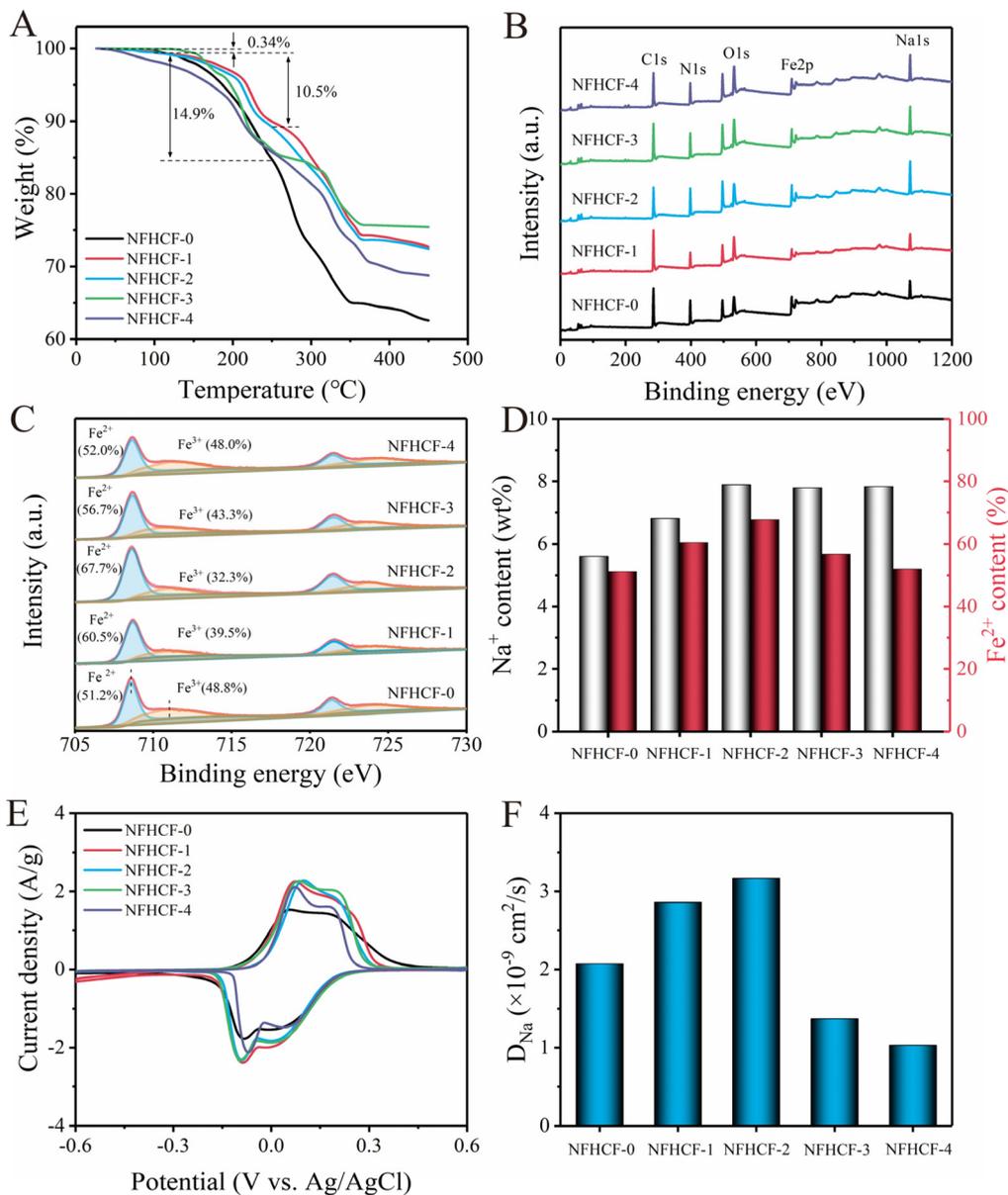
Fig. 2 (A) TGA curves; (B) survey XPS spectra; (C) high-resolution Fe 2p spectra; (D) Na$^+$ content detected by the ICP-OES and Fe^{2+} content detected by the XPS; (E) CV curves at 1 mV s^{-1}; and (F) calculated D_{Na} based on the EIS of NFHCF-x.

for interstitial water content and Fe^{2+} content. Clearly, NFHCF-2 possesses a smaller R_{ct} and the highest D_{Na} thanks to its lower defect degree in the lattice.

These above results suggest that inducing abundant Na$^+$ in the NaFeHCF framework can decrease the crystal vacancies and interstitial water content and enrich the active Fe^{2+}, thus leading to a monoclinic, well-crystalline NaFeHCF with fast charge transfer kinetics.

3.2 Desalination performance

The desalination capabilities of NFHCF-x electrodes were evaluated by the galvanostatic charge–discharge test at 0.25 A g^{-1} (Fig. 3A). NFHCF-2 shows two distinct plateaus at around

−0.05/0.23 V and −0.07/0.19 V, resulting from the redox reactions of Fe^{3+}/Fe^{2+} accompanied by the insertion/de-insertion of Na$^+$.[35] Compared with NFHCF-0 (72.6 mA h g^{-1}), NFHCF-2 exhibits a smaller voltage polarization and higher initial specific capacity (75.0 mA h g^{-1}) due to its monoclinic structure enabled by a low defect degree.

As illustrated in Fig. 3B, NFHCF-0 suffers from poor cycling performance with a capacity retention of only 59.4% after 50 cycles, while the capacity retention of NFHCF-2 can reach 85.3%. This is because NFHCF-2 exhibits higher crystal periodicity and promotes electron/ion transport, which in turn enhances its structural stability during the desalination process. It should be noted that excess NaCl (≥3 M) causes an
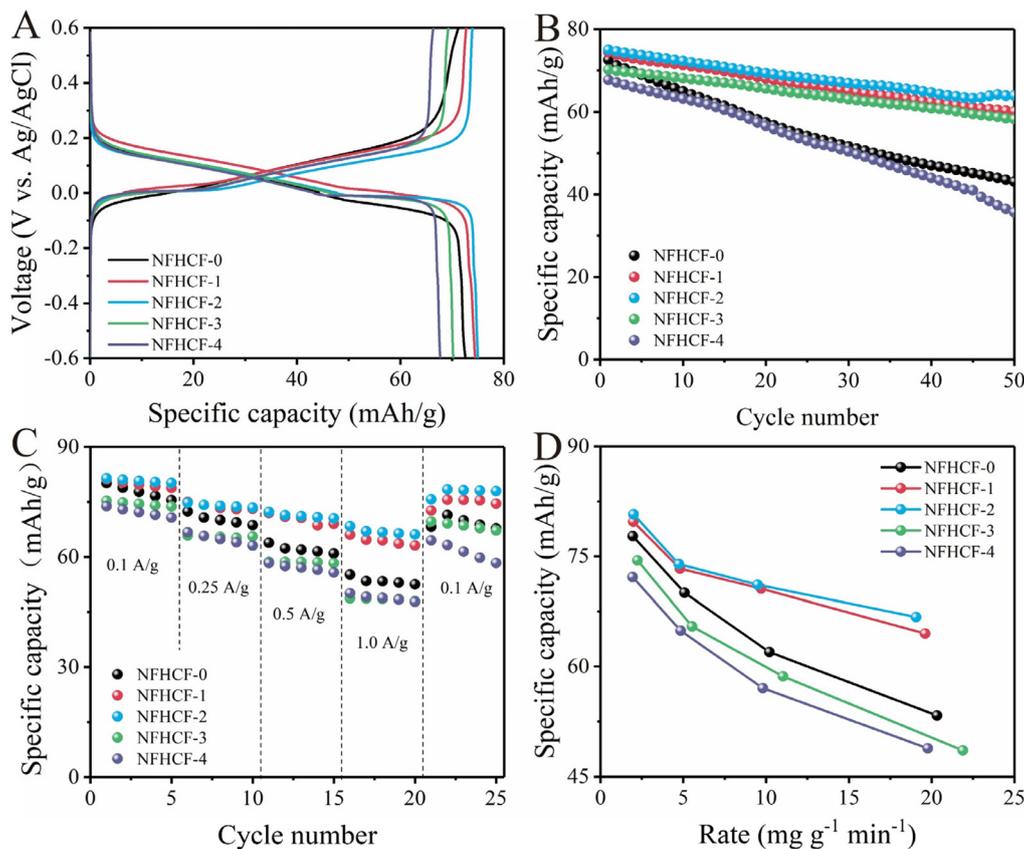
Fig. 3 (A) Initial charge–discharge curves and (B) cycle performance of NFHCF-*x* electrodes at 0.25 A g^{-1}. (C) Rate performance of NFHCF-*x* electrodes. (D) Ragone plot between the desalination capacity and rate of NFHCF-*x* electrodes at different current densities (the calculation of the rate is shown in the ESI†).

increase in the content of vacancies and interstitial water in the NaFeHCF framework, which attenuates its desalination capacity and cycle stability (*e.g.*, for NFHCF-4, the initial specific capacity is 67.7 mA h g^{-1} and capacity retention is 52.7% after 50 cycles). The desalination capacities of NFHCF-*x* were further tested at various current densities (Fig. 3C). NFHCF-2 displays a superior rate capability and delivers a specific capacity of 81.4 mA h g^{-1} at 0.1 A g^{-1}. With the current density increasing to 1.0 A g^{-1}, the specific capacity of 68.4 mA h g^{-1} can still be achieved, corresponding to 83.9% of that at 0.1 A g^{-1}, which is much superior to that of NFHCF-0 (*i.e.*, 68.8%). The Ragone plot between the desalination capacity and rate clearly demonstrates that NFHCF-2 has a larger desalination capacity at a high desalination rate (Fig. 3D).

3.3 Application of symmetrical NFHCF-2-based rocking-chair desalination battery

To further demonstrate the application potential of NFHCF-2, a symmetrical RCDB device was assembled for seawater desalination. The desalination performance of NFHCF-2-based RCDB at different salinities was assessed in NaCl solution in the range of 0.2 to 1.0 M. As the initial NaCl concentration increases, the charge–discharge curves of the NFHCF-2-based RCDB reveal a decrease in voltage polarization (Fig. 4A). The

specific capacity increases from 48.9 mA h g^{-1} for 0.2 M to 63.7 mA h g^{-1} for 1.0 M; meanwhile, the capacity retention increases from 94% to 108.2% after 150 cycles (Fig. 4B).

As shown in Fig. 4C, the solution conductivity decreases with charge and recovers with discharge during the desalination–salination process. According to the change in solution conductivity, the average salt removal capacity (SRC) of NFHCF-2-based RCDB at 0.2 M, 0.4 M, 0.6 M, 0.8 M, and 1.0 M is calculated to be 82.3, 94.4, 96.3, 106.4, and 108.9 mg g^{-1}, respectively. In addition, the corresponding salt removal rate (SRR) is calculated to be 1.87, 1.97, 1.99, 2.16, and 2.22 mg g^{-1} min^{-1}, and the corresponding energy consumption (EC) is calculated to be 0.106, 0.071, 0.058, 0.057, and 0.056 kW h kg^{-1}-NaCl, respectively. To comprehensively evaluate the desalination performance of the NFHCF-2-based RCDB, a radar chart involving five key figures of merit was plotted. As shown in Fig. 4G, each figure of merit also shows an upward trend with the increase in initial NaCl concentration. It can be found that the NFHCF-2-based RCDB has favorable desalination performance and energy consumption at different salinities, especially in high-salinity aqueous media (such as seawater and reverse osmosis brine).

Electrode spacing is of great significance to desalination efficiency in practical applications, as it is a key parameter
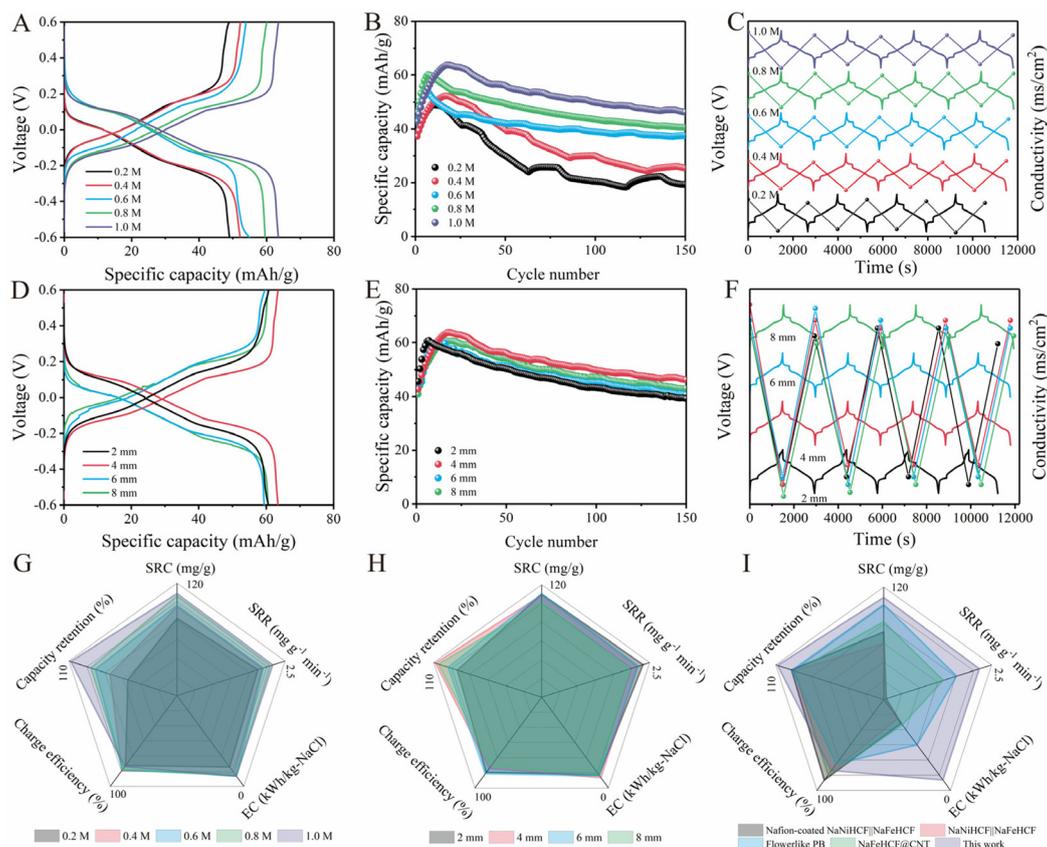
Fig. 4 Charge–discharge curves of NFHCF-2‖NFHCF-2 RCDB after full activation at 0.1 A g^{-1} with (A) various initial NaCl concentrations and (D) various electrode spacings. Cycle performance of NFHCF-2‖NFHCF-2 RCDB with (B) various initial NaCl concentrations and (E) various electrode spacings. Voltage–conductivity curves of NFHCF-2‖NFHCF-2 RCDB at (C) various initial NaCl concentrations and (F) various electrode spacings. Radar chart of NFHCF-2‖NFHCF-2 RCDB at (G) various initial NaCl concentrations and (H) various electrode spacings. (I) Radar chart comparison between NFHCF-2‖NFHCF-2 RCDB and other reported PBA-based RCDBs (detailed information is listed in Table S4†).

affecting energy consumption (through impacting reaction kinetics) and desalination efficiency. Fig. 4D and E reveal the desalination performance of RCDB at various electrode spacings. With electrode spacing decreasing from 8 mm to 4 mm, the ion diffusion distance decreases; thus, the polarization of the RCDB decreases from 0.61 to 0.46 V, the specific capacity increases from 60.6 to 63.7 mA h g^{-1}, and the capacity retention for 150 cycles increases from 105.2% to 108.2%. However, too narrow a spacing (2 mm) will induce greater concentration polarization, which is not conducive to cycle stability during the desalination process (capacity retention decreases to 86%).[36]

As shown in Fig. 4F, the SRC of NFHCF-2-based RCDB at various electrode spacings can be calculated based on the change in solution conductivity, which is 109.9 mg g^{-1} for 2 mm, 108.9 mg g^{-1} for 4 mm, 110.2 mg g^{-1} for 6 mm, and 100.3 mg g^{-1} for 8 mm, respectively. The corresponding SRR and EC are calculated to be 2.35 mg g^{-1} min^{-1} and 0.07 kW h kg^{-1}-NaCl, 2.22 mg g^{-1} min^{-1} and 0.056 kW h kg^{-1}-NaCl, 2.24 mg g^{-1} min^{-1} and 0.067 kW h kg^{-1}-NaCl, as well as 2.02 mg g^{-1} min^{-1} and 0.071 kW h kg^{-1}-NaCl, respectively. Fig. 4H reveals that electrode spacing has a significant effect

on the SRR, EC, and capacity retention of RCDB; moreover, the enclosed area in the radar chart is the largest when the electrode spacing is 4 mm.

The optimal NFHCF-2-based RCDB delivers a large SRC (108.9 mg g^{-1}) with a rapid SRR (2.22 mg g^{-1} min^{-1}), moderate charge efficiency (78.4%), low energy consumption (0.056 kW h kg^{-1}-NaCl), and high cycle stability. As shown in Fig. 4I, the area enclosed by the NFHCF-2-based RCDB in the radar chart is clearly better than that of previously reported PBA-based RCDBs, indicating its great potential for practical applications.[37–40]

To further investigate the technical feasibility of a symmetrical NFHCF-2-based RCDB, desalination experiments were carried out using natural seawater (South China Sea) as an electrolyte, whose composition was analyzed by the ICP-OES test and shown in Table S3.† As shown in Fig. 5A and B, the symmetrical NFHCF-2-based RCDB delivers a specific capacity of 46.2 mA h g^{-1}, and 60.1% of the initial capacity can be retained after 200 cycles with a coulombic efficiency of ~100%. Compared with the NaCl solution, the decrease in desalination performance in natural seawater can be attributed to the dissolved organic matter (*e.g.*, humic acid) and various univalent/bivalent cations (*e.g.*, Na$^+$, Mg^{2+}, Ca^{2+}) contained in natural

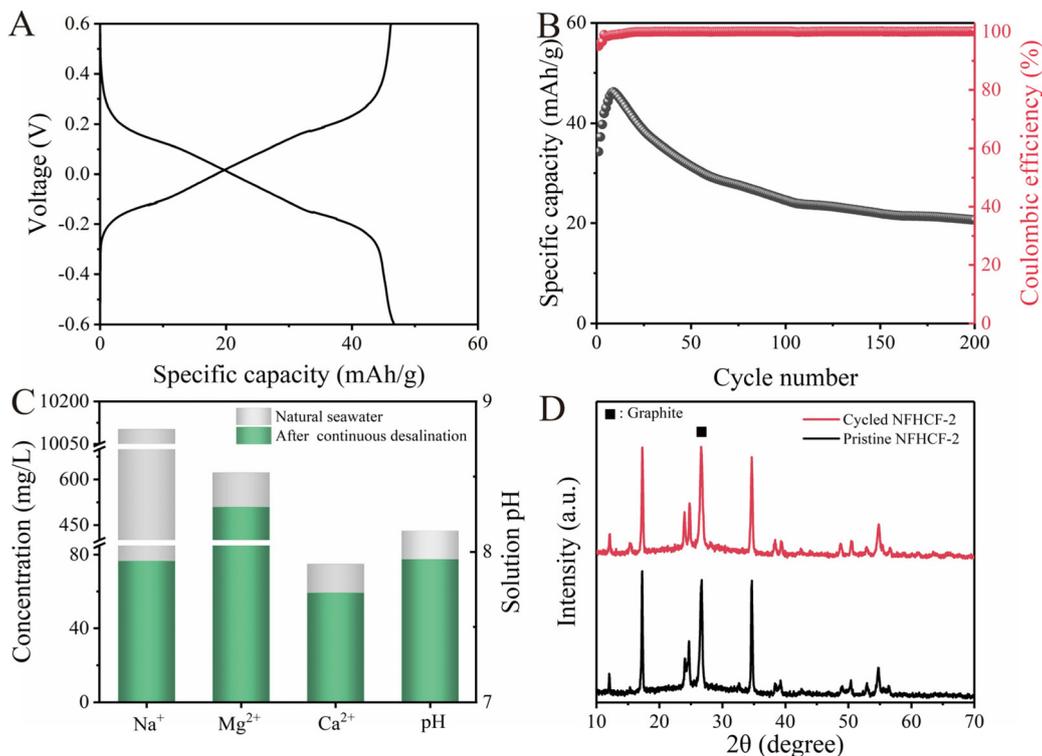**Fig. 5** (A) Charge–discharge curves after full activation and (B) cycle performance of NFHCF-2||NFHCF-2 RCDB in natural seawater at 0.1 A g^{-1}. (C) Various ion removal capacities of NFHCF-2||NFHCF-2 RCDB in natural seawater over consecutive runs. (D) XRD patterns of NFHCF-2 before and after 50 cycles.

seawater. During the desalination process, the organic matter can pollute the surface of electrodes and AEM, hindering the mass transfer process; meanwhile, various univalent/bivalent cations can lead to competitive effects, weakening the ion insertion dynamics of NFHCF.[41,42] As shown in Fig. 5C, after continuous desalination in the RCDB, the ionic concentration in effluent decreases from 10 101.6 to 74.9 mg L^{-1} for Na$^+$, 622.7 to 509.6 mg L^{-1} for Mg^{2+}, and 74.9 to 59.3 mg L^{-1} for Ca^{2+}, with removal rates of 99.2%, 18.2%, and 20.8%, respectively. Meanwhile, only a slight decrease in solution pH and the additional existence of 0.26 mg L^{-1} of Fe ions are detected after long-term operation, implying limited ion leaching during the desalination process. Fig. 5D reveals the XRD patterns of the NFHCF-2 electrode before and after long-term desalination. It can be found that the XRD pattern of the cycled NFHCF-2 electrode has no significant change and still maintains a monoclinic phase structure, which indicates the favorable structural stability of NFHCF-2 in the long-term desalination process.

Based on the above results, the mechanism for ion removal in the symmetrical NFHCF-2-based RCDB is proposed. As shown in Fig. 6, the anode loses electrons during the charging process, resulting in the oxidation of Fe^{2+} in the NFHCF framework to Fe^{3+}, and the cations (e.g., Na$^+$, Mg^{2+}, and Ca^{2+}) are released from the NFHCF to the anode chamber concurrently, while anions (e.g., Cl$^-$) in the cathode chamber pass through the anion-exchange membrane to ensure the electroneutrality
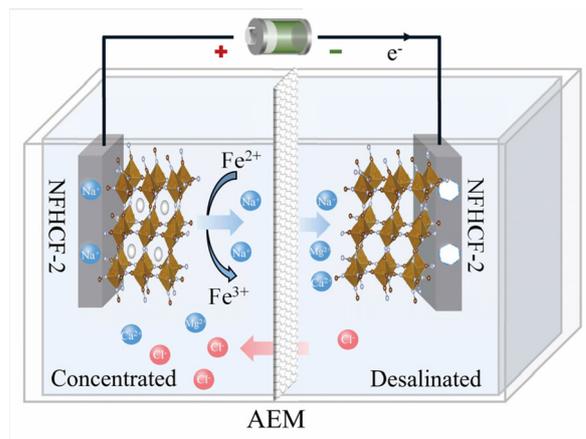

Fig. 6 Schematic illustration of the NFHCF-2||NFHCF-2 RCDB.

of the electrolyte in the anode chamber, thereby producing a concentrated effluent. Following electrons flow into the cathode through the external circuit, Fe^{3+} in the NFHCF framework is reduced to Fe^{2+}, accompanied by cations inserting from the cathode chamber into the electrode, thereby decreasing the salt content of the solution and causing the desalinated effluent. Upon current reversal, the opposite reactions happen in chambers. Therefore, desalinated and concentrated streams can be continuously obtained in the cathode and

anode chambers, respectively. Thanks to the large three-dimensional diffusion channels in the PBA framework, it can accommodate various ions with multiple valence states.[43,44] Herein, the symmetrical NFHCF-2 RCDB can achieve synchronous removal of monovalent/bivalent ions in the natural seawater, which is more suitable for effective desalination of complex natural water matrices.

4 Conclusion

In this work, a series of NaFeHCF samples with tunable defects were successfully synthesized *via* a controlled coprecipitation method. Benefiting from the minimized defect degree, the structurally distorted high-quality monoclinic NFHCF-2 exhibits a high desalination capacity (75.0 mA h g^{-1}) and long cycle stability (capacity retention of 85.3% after 50 cycles). Moreover, a symmetrical NFCHF-2 RCDB with optimized operation parameters delivers an average SRC of 108.9 mg g^{-1} and an SRR of 2.22 mg g^{-1} min^{-1} with moderate charge efficiency (78.4%), low energy consumption (0.056 kW h kg^{-1}-NaCl), and almost no capacity attenuation after 150 cycles, which is superior to previous PBA-based RCDBs. Furthermore, the RCDB system can simultaneously remove univalent/bivalent ions from natural seawater, indicating its potential application prospects in seawater desalination.

Author contributions

Yuliang Wu: methodology, investigation, data curation, software, writing – original draft, visualization; Junkun Huang: methodology, investigation, data curation, software; Chaolin Li: supervision, formal analysis, project administration; Wenhui Wang: conceptualization, methodology, validation, supervision, project administration, writing – review & editing, funding acquisition.

Conflicts of interest

The authors declare that they have no known competing financial interests or personal relationships that could have appeared to influence the work reported in this paper.

Acknowledgements

References

1 K. Kümmerer, D. D. Dionysiou, O. Olsson and D. Fatta-Kassinos, *Science*, 2018, **361**, 222–224.

2 M. Elimelech and W. A. Phillip, *Science*, 2011, **333**, 712–717.

3 Y. Yao, P. Zhang, C. Jiang, R. M. DuChanois, X. Zhang and M. Elimelech, *Nat. Sustain.*, 2021, **4**, 138–146.

4 G. Doornbusch, M. van der Wal, M. Tedesco, J. Post, K. Nijmeijer and Z. Borneman, *Desalination*, 2021, **505**, 114973.

5 H. M. Qiblawey and F. Banat, *Desalination*, 2008, **220**, 633–644.

6 I. Khoshrou, M. R. Jafari Nasr and K. Bakhtari, *Sol. Energy*, 2017, **153**, 115–125.

7 C. Zhang, L. Wu, J. Ma, M. Wang, J. Sun and T. D. Waite, *Water Res.*, 2020, **173**, 115580.

8 F. Yu, H. Yin, X. Bai, J. Pan, X. Zhang and J. Ma, *Chin. Chem. Lett.*, 2023, 108362, DOI: **10.1016/j.cclet.2023.108362**.

9 F. Chen, Y. Huang, L. Guo, M. Ding and H. Y. Yang, *Nanoscale*, 2017, **9**, 10101–10108.

10 D. Xu, W. Wang, M. Zhu and C. Li, *ACS Appl. Mater. Interfaces*, 2020, **12**, 57671–57685.

11 M. Pasta, C. D. Wessells, Y. Cui and F. La Mantia, *Nano Lett.*, 2012, **12**, 839–843.

12 W. Wei, X. Feng, R. Wang, R. Zheng, D. Yang and H. Chen, *Nano Lett.*, 2021, **21**, 4830–4837.

13 X.-J. Dai, X.-X. Niu, W.-Q. Fu, D. Zheng, W.-X. Liu, W.-H. Shi, J.-W. Nai, F.-F. Wu and X.-H. Cao, *Rare Met.*, 2022, **41**, 287–303.

14 Y. Xiong, F. Yu and J. Ma, *Acta Phys.-Chim. Sin.*, 2021, **38**(5), 2006037.

15 D. Xu, W. Wang, M. Zhu and C. Li, *Sep. Purif. Technol.*, 2022, **299**, 121731.

16 K. C. Smith and R. Dmello, *J. Electrochem. Soc.*, 2016, **163**, A530.

17 A. Zhou, W. Cheng, W. Wang, Q. Zhao, J. Xie, W. Zhang, H. Gao, L. Xue and J. Li, *Adv. Energy Mater.*, 2021, **11**, 2000943.

18 J. Qian, C. Wu, Y. Cao, Z. Ma, Y. Huang, X. Ai and H. Yang, *Adv. Energy Mater.*, 2018, **8**, 1702619.

19 Z. Hao, X. Sun, J. Chen, X. Zhou and Y. Zhang, *Small*, 2023, 2300253.

20 C. Xu, Z. Yang, X. Zhang, M. Xia, H. Yan, J. Li, H. Yu, L. Zhang and J. Shu, *Nano-Micro Lett.*, 2021, **13**, 166.

21 Z. Tang, B. Hu, P. Nie, X. Shang, J. Yang and J. Liu, *Chem. Eng. J.*, 2023, **466**, 143216.

22 X. Zhang and J. Dutta, *ACS Appl. Energy Mater.*, 2021, **4**, 8275–8284.

23 S. Wang, Z. Pan, Z. Li, H. Zhuang, L. Zhao, Z. Li, Y. Lei and G. Wang, *Chem. Eng. J.*, 2023, **466**, 143163.

24 J. Guo, Y. Wang, H. Zhang, Y. Cai and R. Fang, *Desalination*, 2023, **548**, 116305.

25 W. Shi, X. Liu, T. Deng, S. Huang, M. Ding, X. Miao, C. Zhu, Y. Zhu, W. Liu, F. Wu, C. Gao, S.-W. Yang, H. Y. Yang, J. Shen and X. Cao, *Adv. Mater.*, 2020, **32**, 1907404.

26 S. Wang, Z. Li, G. Wang, Y. Wang, Z. Ling and C. Li, *ACS Nano*, 2022, **16**, 1239–1249.

27 H. Yi, R. Qin, S. Ding, Y. Wang, S. Li, Q. Zhao and F. Pan, *Adv. Funct. Mater.*, 2021, **31**, 2006970.

28 Y. Yang, E. Liu, X. Yan, C. Ma, W. Wen, X.-Z. Liao and Z.-F. Ma, *J. Electrochem. Soc.*, 2016, **163**, A2117.

29 M. Qin, W. Ren, R. Jiang, Q. Li, X. Yao, S. Wang, Y. You and L. Mai, *ACS Appl. Mater. Interfaces*, 2021, **13**, 3999–4007.

30 Y. Xu, J. Wan, L. Huang, M. Ou, C. Fan, P. Wei, J. Peng, Y. Liu, Y. Qiu, X. Sun, C. Fang, Q. Li, J. Han, Y. Huang, J. A. Alonso and Y. Zhao, *Adv. Energy Mater.*, 2019, **9**, 1803158.

31 J. Song, L. Wang, Y. Lu, J. Liu, B. Guo, P. Xiao, J.-J. Lee, X.-Q. Yang, G. Henkelman and J. B. Goodenough, *J. Am. Chem. Soc.*, 2015, **137**, 2658–2664.

32 Y. Liu, Y. Qiao, W. Zhang, Z. Li, X. Ji, L. Miao, L. Yuan, X. Hu and Y. Huang, *Nano Energy*, 2015, **12**, 386–393.

33 J. Peng, J. Huang, Y. Gao, Y. Qiao, H. Dong, Y. Liu, L. Li, J. Wang, S. Dou and S. Chou, *Small*, 2023, 2300435.

34 H. Li, X. Ding, J. Shi, M. Su, Y. Hu, C. Zhang, F. Gao and Q. Lu, *Small*, 2023, **19**, 2207525.

35 A. Gong, Y. Zhao, M. He, B. Liang and K. Li, *Desalination*, 2021, **505**, 114997.

36 P. Długołȩcki, A. Gambier, K. Nijmeijer and M. Wessling, *Environ. Sci. Technol.*, 2009, **43**, 6888–6894.

37 X. Wei, Y. Zhao, B. Liang, X. Mo and K. Li, *Sep. Purif. Technol.*, 2021, **266**, 117899.

38 J. Ahn, S. Kim, S.-I. Jeon, C. Lee, J. Lee and J. Yoon, *Desalination*, 2021, **500**, 114778.

39 J. Lee, S. Kim and J. Yoon, *ACS Omega*, 2017, **2**, 1653–1659.

40 X. Tu, Y. Liu, K. Wang, Z. Ding, X. Xu, T. Lu and L. Pan, *J. Colloid Interface Sci.*, 2023, **642**, 680–690.

41 J. Shim, N. Yoon, S. Park, J. Park, M. Son, K. Jeong and K. H. Cho, *Chemosphere*, 2021, **264**, 128519.

42 Y. Li, C. Zhang, Y. Jiang, T.-J. Wang and H. Wang, *Desalination*, 2016, **399**, 171–177.

43 E. Sebti, M. M. Besli, M. Metzger, S. Hellstrom, M. J. Schultz-Neu, J. Alvarado, J. Christensen, M. Doeff, S. Kuppan and C. V. Subban, *Desalination*, 2020, **487**, 114479.

44 K. Singh, Z. Qian, P. M. Biesheuvel, H. Zuilhof, S. Porada and L. C. P. M. de Smet, *Desalination*, 2020, **481**, 114346.